The Astrophysical Journal, 650:1096–1110, 2006 October 20

MEASUREMENTS AND ANALYSIS OF HELIUM-LIKE TRIPLET RATIOS IN THE X-RAY SPECTRA OF O-TYPE STARS

Maurice A. Leutenegger and Frits B. S. Paerels
Department of Physics and Columbia Astrophysics Laboratory, Columbia University, 550 West 120th Street, New York, NY 10027; maurice@astro.columbia.edu

Steven M. Kahn
Kavli Institute for Particle Astrophysics and Cosmology, Stanford Linear Accelerator Center and Stanford University, 2575 Sand Hill Road, Menlo Park, CA 94025

and

David H. Cohen
Department of Physics and Astronomy, Swarthmore College, 500 College Avenue, Swarthmore, PA 19081
Received 2005 December 6; accepted 2006 June 14

ABSTRACT

We discuss new methods of measuring and interpreting the forbidden-to-intercombination line ratios of helium-like triplets in the X-ray spectra of O-type stars, including accounting for the spatial distribution of the X-ray-emitting plasma and using the detailed photospheric UV spectrum. Measurements are made for four O stars using archival *Chandra* HETGS data. We assume an X-ray-emitting plasma spatially distributed in the wind above some minimum radius R_0. We find minimum radii of formation typically in the range of $1.25 < R_0/R_* < 1.67$, which is consistent with results obtained independently from line profile fits. We find no evidence for anomalously low f/i ratios, and we do not require the existence of X-ray-emitting plasmas at radii that are too small to generate sufficiently strong shocks.

Subject headings: stars: early-type — stars: winds, outflows — techniques: spectroscopic

Online material: color figures

1. INTRODUCTION

Since the discovery of X-ray emission from OB stars by *Einstein* (Harnden et al. 1979; Seward et al. 1979), the exact mechanism for X-ray production has been something of a mystery. X-ray emission from OB stars had been predicted by Cassinelli & Olson (1979), who proposed that an X-ray-emitting corona could explain the observation of superionized O VI through Auger ionization of O IV. However, subsequent observations showing less attenuation of soft X-rays than would be expected from a corona lying below a dense stellar wind made a purely coronal origin seem unlikely (Cassinelli & Swank 1983). Macfarlane et al. (1993) also found that a distributed X-ray source was necessary to explain the observed O VI ultraviolet (UV) P Cygni profile in ζ Pup. Furthermore, with no expectation of a solar-type α-Ω dynamo in OB stars with radiative envelopes, the coronal model fell out of favor. Subsequently, several scenarios in which magnetic field generation and dynamos could exist in OB stars have been proposed (Charbonneau & MacGregor 2001; MacGregor & Cassinelli 2003; Mullan & MacDonald 2005). Since these models have been proposed, the primary observational evidence invoked by their proponents is anomalously low f/i ratios in the X-ray emission of a few helium-like ions in several stars. Reexamining these line ratios and determining whether they require a coronal model to explain them is one of the main goals of this paper.

Shocks arising from instabilities in the star's radiatively driven wind have been considered to provide a more likely origin for the observed X-ray emission, as they are expected to be present, given the line-driven nature of these winds (Lucy & White 1980; Lucy 1982; Krolik & Raymond 1985; Owocki et al. 1988; Feldmeier 1995). However, there have been difficulties in reproducing the observed X-ray properties of O stars, such as the overall X-ray luminosity and the spectral energy distribution, from stellar wind instability models (Hillier et al. 1993; Feldmeier 1995; Feldmeier et al. 1997a, 1997b). Until recently, the quality of the available spectral data provided little insight into these problems, since the CCD and proportional counter spectra could not resolve individual spectral lines.

Recent high-resolution X-ray spectroscopy of OB stars by the *XMM-Newton* Reflection Grating Spectrometer (RGS; Kahn et al. 2001; Mewe et al. 2003; Raassen et al. 2005) and the *Chandra* High Energy Transmission Grating Spectrometer (HETGS; Schulz et al. 2000; Waldron & Cassinelli 2001, hereafter WC01; Cassinelli et al. 2001; Miller et al. 2002; Cohen et al. 2003, 2006; Kramer et al. 2003; Gagné et al. 2005) have answered some questions while raising new ones. Some stars have X-ray spectra that appear consistent with emission from shocks in the wind, but the detailed comparisons to predicted spectral models are still problematic. Both WC01 and Cassinelli et al. (2001) have found low forbidden-to-intercombination line ratios in one set of helium-like triplets each in the X-ray spectra of ζ Ori and ζ Pup. They infer from this that some of the X-ray-emitting plasma is too close to the star to allow shocks of sufficient velocity to develop.

Other stars (θ^1 Ori C and τ Sco) have X-ray spectra that are unusually hard and have relatively small line widths. While these stars might be considered prime candidates for a coronal model of X-ray emission, especially after having magnetic fields detected via Zeeman splitting (Donati et al. 2002, 2006), their behavior is better understood in terms of the magnetically channeled wind-shock model, rather than a model of magnetic heating (Schulz et al. 2000, 2003; Cohen et al. 2003; Gagné et al. 2005; Donati et al. 2006).

Finally, we note that for all of the O giants and supergiants observed, the line profiles are less asymmetric than predicted, given the high mass-loss rates measured for these stars using

TABLE 1
PARAMETERS ADOPTED FOR He-LIKE TRIPLET

Ion	f[a]	λ_1[a] (Å)	λ_2[a] (Å)	ϕ_c (s^{-1})[b]	$\mathcal{R}_0$[c]	$G(T_{max})$[c]
S XV	0.0507	738.32	673.40	9.16E5	2.0	...
Si XIII	0.0562	865.14	814.69	2.39E5	2.3	0.68
Mg XI	0.0647	1034.31	997.46	4.86E4	2.7	0.71
Ne IX	0.0700	1272.81	1248.28	7.73E3	3.1	0.74
O VII	0.0975	1638.28	1623.61	7.32E2	3.7	0.90
N VI	0.1136	1907.26	1896.74	1.83E2	5.3	0.88

[a] Oscillator strengths and transition wavelengths are from CHIANTI (Dere et al. 1997; Young et al. 2003). The oscillator strength is for the sum of all three transitions $2\,^3S_1 \rightarrow 2\,^3P_J$, and $\lambda_{1,2}$ are the transition wavelengths for $2\,^3S_1 \rightarrow 2\,^3P_{1,2}$, respectively.
[b] Data for ϕ_c are from BDT72.
[c] Data for $\mathcal{R}_0$ and $G(T_{max})$ are from Porquet et al. (2001), except S XV, which is from BDT72.

radio free-free emission, Hα emission, and UV absorption lines (WC01; Kahn et al. 2001; Cassinelli et al. 2001; Miller et al. 2002; Kramer et al. 2003; Cohen et al. 2006). This implies either a lower effective opacity to X-rays in their winds (e.g., due to clumping or porosity effects; Feldmeier et al. 2003; Oskinova et al. 2004, 2006; Owocki & Cohen 2006) or lower mass-loss rates (Crowther et al. 2002; Massa et al. 2003; Hillier et al. 2003; Bouret et al. 2005; Fullerton et al. 2006).

One of the key diagnostic measurements available to us in understanding the nature of X-ray emission in OB stars is the forbidden-to-intercombination line ratio in the emission from ions that are isoelectronic with helium. This ratio is sensitive to the UV flux, and thus to the proximity to the stellar surface. This allows us to constrain the location of the X-ray-emitting plasma independently of other spectral data, such as emission line profile shapes.

In this paper we discuss methods for using the f/i ratio to constrain the location of X-ray-emitting plasma in O-star winds. In particular, we explore the effects of a spatially distributed source motivated by the broad line profiles. We discuss the effects of photospheric absorption lines, as well as the f/i ratio expected for a plasma emitted over a range of radii, taking account of detailed line shapes when signal-to-noise ratio allows. We find that accounting in detail for photospheric absorption lines is not important, as long as the X-ray emission originates over a range of radii.

These methods are then applied to helium-like triplet emission in a set of archival *Chandra* observations of O stars. Our primary result is that good fits can be achieved for most lines with models having emission distributed over the wind, with minimum radii of about 1.5 stellar radii. We find that none of the data require the X-ray-emitting plasma to be formed very close to the photosphere.

This paper is organized as follows. In § 2 we review the physics of line formation in helium-like species (§ 2.1) and explore the effects of spectral structure in the photoexciting UV field (§ 2.2) and spatial distribution of the X-ray-emitting plasma (§ 2.3), while incorporating the line-ratio modeling into a self-consistent line profile model (§ 2.4). In § 3 we discuss the reduction and analysis of archival O-star X-ray spectra. In § 4 we give the results of this analysis, fitting high signal-to-noise ratio complexes with the self-consistent line profile model described in § 2.4 and fitting the lower signal-to-noise ratio complexes with multiple Gaussians and interpreting these results according to the spatially distributed picture described in § 2.3. In § 5 we discuss the implications of these results, and in § 6 we give our conclusions.

2. MODEL

2.1. *Radial Dependence of the f/i Ratio*

The physics of helium-like ions in coronal plasmas has been investigated in numerous papers (Gabriel & Jordan 1969, hereafter GJ69; Blumenthal et al. 1972, hereafter BDT72; Gabriel & Jordan 1973; Mewe & Schrijver 1975, 1978a, 1978b, 1978c; Pradhan & Shull 1981; Pradhan 1982; Porquet et al. 2001). The principal diagnostic is the ratio of the strengths of the forbidden to intercombination lines, $\mathcal{R} \equiv f/i$. We use the calligraphic $\mathcal{R}$ to refer to this ratio, and the italic R to refer to distances comparable to the stellar radius.

The upper level of the forbidden line ($2\,^3S_1$) is metastable and relatively long-lived. When the excitation rate from $2\,^3S_1$ to the upper levels of the intercombination line ($2\,^3P_{1,2}$) becomes comparable to the decay rate of the forbidden transition, the line ratio is altered.[1] The excitations may be due to electron impacts in a high-density plasma, or due to an external UV radiation source.

GJ69 and BDT72 derive the expression

$$\mathcal{R} = \mathcal{R}_0 \frac{1}{1 + \phi/\phi_c + n_e/n_c}, \quad (1)$$

where ϕ is the photoexcitation rate from $2\,^3S$ to $2\,^3P$ and ϕ_c is the critical rate at which $\mathcal{R}$ is reduced to $\mathcal{R}_0/2$. Similarly, n_e is the electron density, and n_c is the critical density.

In Table 1 we give our adopted values for the atomic parameters necessary for calculation of helium-like triplet ratios. We adopt the BDT72 values for ϕ_c, because they have calculated it for all the ions we are interested in and because more recent calculations are not substantially different. However, we use the more recent values for $\mathcal{R}_0$ from Porquet et al. (2001); their calculations of $\mathcal{R}_0$ are slightly lower than those of BDT72. Porquet et al. (2001) also give values for $G \equiv (f + i)/r$, evaluated at T_{max}, the temperature at which emission from that helium-like ion is the strongest. We cite $G(T_{max})$ for comparison with our measurements.

Because densities high enough to cause a change in the line ratios exist only very close to the star, we consider only the photoexcitation term. If there are O stars with f/i ratios that are measured to be too low to be explained by photoexcitation, it is appropriate to consider the effects of high density; this is not the case for any of our measurements.

[1] The $2\,^3S_1$ state may also be excited to the $2\,^3P_0$ state, but this state does not decay to ground, so we omit it from our discussion. However, in GJ69 and BDT72 the formal treatment involves all states.

TABLE 2
ADOPTED STELLAR PARAMETERS

Star	Spectral Type[a]	$T_{\rm eff}$ (kK)[b]	$\log g$ (cm s^{-2})[b]	v_∞ (km s^{-1})[c]
ζ Pup	O4 I	42.5	3.75	2485
ζ Ori	O9.5 I	30.0	3.25	1860
ι Ori	O9 III	35.0	3.50	2195
δ Ori	O9.5 II	32.5	3.25	1995

[a] Spectral types are given for reference and are taken from the Garmany values reported in Table 1 of Lamers & Leitherer (1993).
[b] Effective temperatures and surface gravities are the values on the TLUSTY O-star grid that are the closest approximations to the values used in Lamers & Leitherer (1993).
[c] Terminal velocities are taken from Prinja et al. (1990).

The expression for ϕ may be evaluated as follows, given a model stellar atmosphere Eddington flux H_ν,

$$\phi = \frac{16\pi^2 e^2}{m_e c} f \frac{H_\nu}{h\nu} W(r), \tag{2}$$

where $W(r) = \frac{1}{2}\{1 - \left[1 - (R_*/r)^2\right]^{1/2}\}$ is the geometrical dilution.

The expression for the $\mathcal{R}$ ratio derived by GJ69 is written such that f is the sum of the oscillator strengths for $2\ ^3S_1$ to all three of $2\ ^3P_J$, despite the fact that $2\ ^3P_0$ does not decay to ground, and $2\ ^3P_2$ only contributes for high Z. For low Z (Ne IX and lower) H_ν should be evaluated for $2\ ^3S_1 \rightarrow 2\ ^3P_1$. For Mg XI and higher Z ions it is more accurate to evaluate H_ν for both $2\ ^3S_1 \rightarrow 2\ ^3P_1$ and $2\ ^3P_2$ and weight the average by the relative contributions to the effective branching ratio. Of course, this is only necessary if H_ν is substantially different for the two transitions.

Since the flux of UV radiation seen by ions in a stellar wind decreases in proportion to the geometrical dilution factor $W(r)$, the $\mathcal{R}$ ratio is also a function of radius. It is helpful to express it in this form,

$$\mathcal{R}(r) = \mathcal{R}_0 \frac{1}{1 + 2P\,W(r)}, \tag{3}$$

where $P = \phi_*/\phi_c$ and

$$\phi_* = 8\pi \frac{\pi e^2}{m_e c} f \frac{H_\nu}{h\nu}. \tag{4}$$

The value of the $\mathcal{R}$ ratio near the photosphere is then $\mathcal{R}_{\rm ph} = \mathcal{R}_0/(1 + P)$.

In this paper we perform calculations and make measurements for a sample of four O stars observed by *Chandra*: ζ Pup, ζ Ori, ι Ori, and δ Ori. The relevant properties of these stars are given in Table 2. The effective temperatures and gravities of the stars are taken from Lamers & Leitherer (1993) and then rounded off to the closest values calculated on the TLUSTY O-star grid (Lanz & Hubeny 2003).

2.2. *The Effect of Photospheric Absorption Lines*

The expression for $\mathcal{R}(r)$ written in the previous paragraph involves an approximation that must be explored further. We assumed a photospheric UV flux that would be diluted by geometry, but we neglected the Doppler shift of the absorbing ions. Over the range of Doppler shifts seen in a stellar wind, there can be many photospheric absorption lines. This introduces an additional radial dependence to the photoexcitation rate, and thus the $\mathcal{R}$ ratio,

$$\phi(r) \propto H_{\nu(r)} W(r), \tag{5}$$

where the Doppler-shifted frequency as seen by an ion at radius r is

$$\nu(r) = \nu_0 \left[1 + \frac{v(r)}{c}\right]. \tag{6}$$

In this expression a positive velocity represents a blue shift.

In Figure 1 we show a plot of the photospheric UV flux for a model representing ζ Ori near the $2\ ^3S_1 \rightarrow 2\ ^3P_{1,2}$ transitions of Mg XI. The model is taken from the TLUSTY O-star model grid (Lanz & Hubeny 2003). Note that for Mg XI, most of the intercombination line strength still arises from the $2\ ^3P_1$ to ground transition.

We also compute the $\mathcal{R}$ ratio using an averaged value of H_ν, which we compare to the $\mathcal{R}$ ratio calculated using the nonaveraged (radially dependent) H_ν. We do this to understand whether it is important to explicitly account for photospheric absorption lines or it is sufficient to calculate $\mathcal{R}$ using an averaged value of the photospheric UV flux. We use the average value of H_ν over the range $0.1 < \mathcal{R}/\mathcal{R}_0 < 0.9$, or $9 > 2P\,W(r) > 0.111$. There are two reasons for this: when the photoexcitation rate is much less than the critical rate, the effect of photospheric lines on $\mathcal{R}$ is small, and when the photoexcitation rate is so high that the forbidden line is very weak, we cannot measure variations in the forbidden line strength. We estimate this range using the continuum UV flux. In cases in which $\mathcal{R}$ does not ever get reduced to $0.1\mathcal{R}_0$ (even at the photosphere) because the UV flux is not strong enough, we average from the rest frequency to the frequency at which $\mathcal{R} = 0.9\mathcal{R}_0$.

In Figure 2 we show $\mathcal{R}(r)$ for averaged (*lower dashed line*) and nonaveraged (*lower solid line with fluctuations*) H_ν for Mg XI for the star ζ Ori. There are substantial fluctuations in $\mathcal{R}(r)$ for the nonaveraged case. The two upper lines in the figure are discussed in § 2.3; they represent the effects of averaging the emission over a range of radii, as opposed to simply over a range of frequencies.

In making this figure we have ignored all additional Doppler shifts, as the purpose of the plot is mainly to illustrate qualitatively the effect of photospheric absorption lines on the $\mathcal{R}$ ratio. Examples of potentially relevant Doppler shifts are the thermal velocities of the ions (of order 100 km s^{-1} for neon at 0.4 keV), stellar rotation (typically 100–200 km s^{-1} for O-type stars, although the wind also rotates), and the nonmonotonicity of the stellar wind due to shocks (e.g., Feldmeier [1995], of order a few 100 km s^{-1}). We have also treated the star as a point source rather than a finite disk, which would change the projected velocity as a function of position on the stellar disk. All of these effects are small compared to the wind terminal velocity, but they could diminish the impact of photospheric lines on the f/i ratio by smearing out the photospheric spectrum.

One possibly important effect we neglect is scattering by resonance lines of ions in the wind. This is probably relevant only for Mg XI. In this case the O VI line at 1031.91 Å is on the blue side of

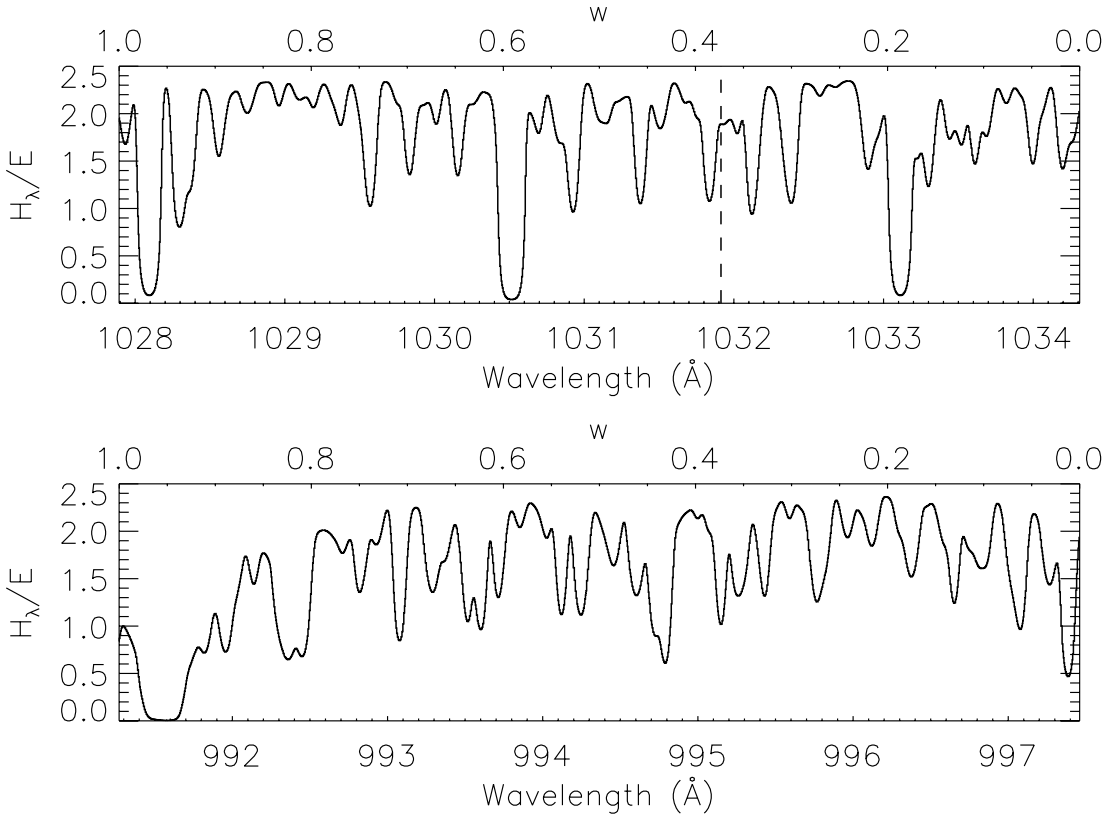

FIG. 1.—Model UV flux for ζ Ori near the $2\ ^3S_1 \rightarrow 2\ ^3P_{1,2}$ transitions of Mg XI ($J = 1$, *top*; $J = 2$, *bottom*), plotted as a function of wavelength (*bottom axis*) and scaled stellar wind velocity, $w(u) = v(u)/v_\infty$ (*top axis*). The flux is given in units of 10^{20} photons cm^{-2} s^{-1} Å^{-1}. The dashed line shows the rest wavelength of the O VI line at 1031.91 Å. For comparison the average continuum flux we use for this ion and this star is 1.67, in the same units. The model flux is taken from the TLUSTY O-star grid (Lanz & Hubeny 2003).

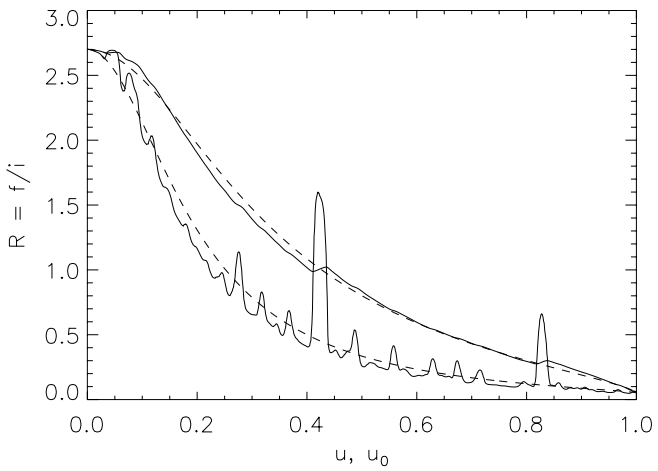

FIG. 2.—The f/i ratio for the Mg XI triplet of ζ Ori plotted as a function of the inverse radial coordinate $u = R_*/r$. The solid lines are for the actual model photospheric UV flux, while the dashed lines are for an averaged value. The bottom pair of lines show the local radial dependence of $\mathcal{R}(u)$; the top pair of lines show the integrated ratio $\overline{\mathcal{R}}(u_0)$ observed for the whole star (see text). Note that u and u_0 are not comparable physical quantities, since u corresponds to a single radius, which could be interpreted as a characteristic radius, while u_0 corresponds to the *minimum* radius for the onset of X-ray emission. The solid lines include the effects of the photospheric UV flux for transitions to both the $2\ ^3P_1$ and $2\ ^3P_2$ states, although the $2\ ^3P_1$ state is far more important for Mg XI. The peaks in the bottom solid line correspond to the absorption lines in the top panel of Fig. 1. [*See the electronic edition of the Journal for a color version of this figure*.]

the $2\ ^3S_1 \rightarrow 2\ ^3P_1$ transition at 1034.31 Å, which means that it could scatter the UV light from the photosphere to a different wavelength. However, it is not clear that this will greatly affect the line ratio, as the scattering process does not generally destroy photons. The detailed effects of scattering by this transition could be assessed by modeling the radiative transfer in the wind at this wavelength range, but this is beyond the scope of this work.

2.3. *The Integrated Ratio*

In §§ 2.1 and 2.2 we calculated the radial dependence of the f/i ratio. Here, we calculate the f/i ratio integrated over an emitting volume that may span a wide range of radii. After all, for any realistic model of a stellar wind, we expect the X-ray-emitting plasma to be distributed over a large range of radii (although it could be a small range of radii for a coronal model). We cannot directly observe the ratio as a function of radius, but only the overall ratio, or the ratio as a function of the observed Doppler shift.

We make the simple assumptions that the emissivity of the X-ray-emitting plasma scales as the wind density squared above some onset radius. This is the same set of assumptions as the model of Owocki & Cohen (2001, hereafter OC01), with the two additional simplifications that there is no continuum absorption and that there is no radial variation in the X-ray filling factor. These approximations are not unreasonable, considering the low characteristic optical depths and the radial dependence of the filling factor reported by Kramer et al. (2003) for fits to line profiles in the *Chandra* HETGS spectrum of ζ Pup, especially for high Z, where the optical depths are expected to be smallest.

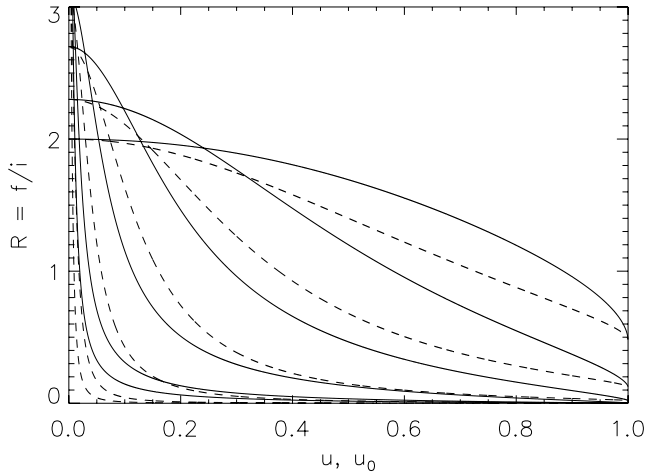

FIG. 3.—The f/i ratio for six helium-like triplets observed in ζ Pup. The dashed lines show the radial dependence of $\mathcal{R}$, while the solid lines show the dependence of the integrated ratio $\overline{\mathcal{R}}$ on the inverse minimum radius $u_0 = R_*/R_0$. The curves fall in increasing order of Z from left to right. S XV is omitted from the subsequent three figures because it is not observed in the spectra of those stars. [*See the electronic edition of the Journal for a color version of this figure.*]

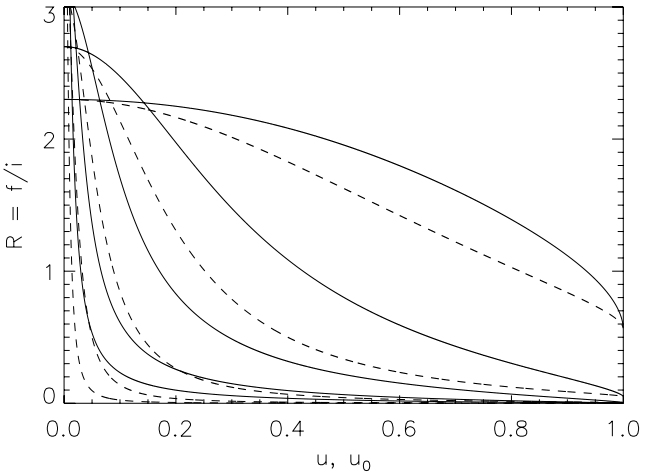

FIG. 4.—Same as Fig. 3, but for five helium-like triplets observed in ζ Ori. [*See the electronic edition of the Journal for a color version of this figure.*]

To calculate the integrated strength of the forbidden and intercombination lines, we weight the integrand with the normalized (radially dependent) strength of each line.[2] The weights are

$$f(u) = G\frac{\mathcal{R}(u)}{1+\mathcal{R}(u)}, \tag{7}$$

and

$$i(u) = G\frac{1}{1+\mathcal{R}(u)}, \tag{8}$$

where $u \equiv R_*/r$ is the inverse radial coordinate. We have introduced $G \equiv (\text{for} + \text{int})/\text{res}$ to ensure that the weighting factors are properly normalized relative to the resonance line; we discuss this in more detail in § 2.4. The radial dependence of $\mathcal{R}(u)$ was discussed in the previous sections (see eq. [3]).

The integrated ratio is then

$$\overline{\mathcal{R}}(u_0) = \frac{\int dV\,\eta_f}{\int dV\,\eta_i}, \tag{9}$$

where $\eta_{f,i}$ are the emissivities of the forbidden and intercombination lines. The integrals are

$$\int dV\,\eta_{f,i} \propto \int_{R_0}^{\infty} \Omega(r) r^2\,dr \rho^2(r) f,i(r) \propto \int_0^{u_0} \frac{du\,\Omega(u)}{w^2(u)} f,i(u), \tag{10}$$

where we have used $\rho(u) \propto u^2/w(u)$. The term $\Omega(u) = 2\pi[1 + (1-u^2)^{1/2}]$ is the solid angle visible by the observer (i.e., not obscured by the stellar core). The term $w(u) = v(u)/v_\infty = (1-u)^\beta$ is the scaled velocity; we take $\beta = 1$ as a convenient approximation, as discussed in § 2.4. The limit R_0 is the onset radius for X-ray emission, and $u_0 = R_*/R_0$ is its inverse. The helium-like line-strength weights $f,i(u)$ are given by equations (7) and (8), respectively.

In Figure 2, the top two lines show the integrated f/i ratio as a function of u_0 for Mg XI in ζ Ori. The integrated ratio is very similar for both the averaged (*top dashed line*) and unaveraged (*top solid line*) cases. Since it is much simpler to consider only a single value of photospheric UV flux and because it agrees well with the more detailed treatment, we do so in the rest of this paper. However, it should be noted that if one modeled the X-ray emission as arising near a single radius or Doppler shift, as might be appropriate for a coronal model, the actual photospheric flux (including absorption lines) would need to be included in the modeling.

It is important to note that there are two separate physical effects being considered here. The first is the effect of using the actual photospheric spectrum instead of a wavelength average, and the second is the averaging of the $\mathcal{R}$ ratio over a range of radii. What Figure 2 shows is that the first effect is not important if we include the second. However, when comparing the radius inferred from a localized model to the *minimum* radius inferred from the distributed model, it is crucial to realize that they are physically different quantities. The radius in a localized model can be taken literally as the characteristic location of the X-ray-emitting plasma, but in the distributed model the minimum

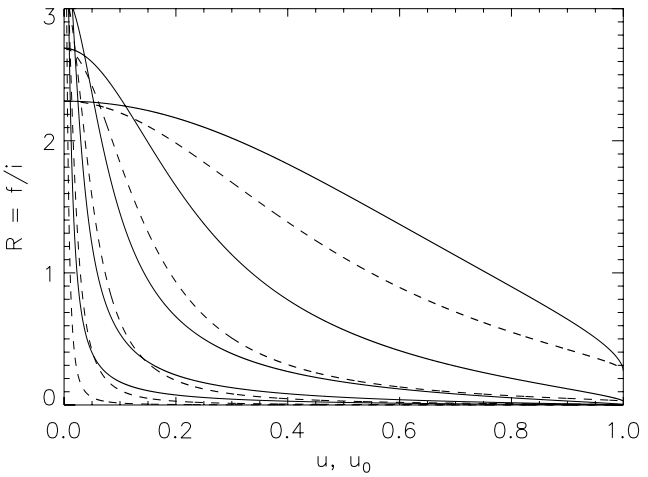

FIG. 5.—Same as Fig. 3, but for five helium-like triplets observed in ι Ori. [*See the electronic edition of the Journal for a color version of this figure.*]

[2] We could instead express the integrated ratio as a single volume integral of the f/i ratio with a weighting term for the overall emissivity of the complex, but we feel that the formalism we use here, of a ratio of two separate emissivity integrals, is more intuitive. However, the two methods are formally equivalent.

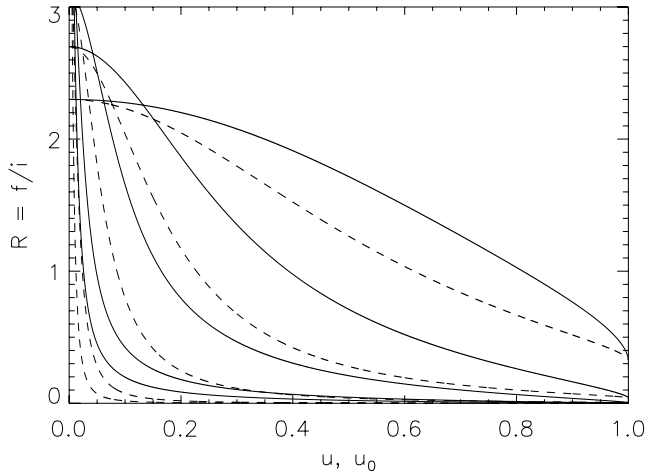

FIG. 6.—Same as Fig. 3, but for five helium-like triplets observed in δ Ori. [*See the electronic edition of the Journal for a color version of this figure*.]

radius is the smallest radius where there is X-ray emission; it can be interpreted physically as the shock onset radius.

In Figures 3–6 we show $\mathcal{R}(u)$ and $\overline{\mathcal{R}}(u_0)$ for all helium-like ions observed in the four O stars we consider in this paper. These plots all assume an averaged value of the photospheric UV flux. For a given measured value of $\mathcal{R}$, there are substantial differences between the value of u_0 derived assuming a distributed plasma and the value of u derived assuming a plasma dominated by one radius; that is, u_0 is always larger than u for a single radius, as one would expect.

In Table 3 we compare our calculations using TLUSTY model stellar atmosphere fluxes to the same calculations using Kurucz (1979) fluxes, as in WC01 and Cassinelli et al. (2001). We make the comparison for one key ion for each paper, both of which have their $2\ ^3S_1 \rightarrow 2\ ^3P_J$ transition wavelengths in the Lyman continuum. We use $\mathcal{R}_0$ values taken directly from the plots of WC01 and Cassinelli et al. (2001). For most ions in these two papers, $\mathcal{R}_0$ is taken from BDT72, but for Si XIII, WC01 use $\mathcal{R}_0 = 2.85$, while the BDT72 value is 2.51. The values of $\mathcal{R}_0$ given in BDT72 are systematically higher than those in Porquet et al. (2001).

There are substantial differences between our calculations of $\mathcal{R}_{\rm ph}$ (the value of $\mathcal{R}$ at the photosphere) and those of WC01, Cassinelli et al. (2001), and Miller et al. (2002). These differences mainly arise from differences in the continuum flux of the photospheric models shortward of the Lyman edge; the TLUSTY models generally predict a factor of 2–3 more than the Kurucz models.

The combination of the different Lyman continua and $\mathcal{R}_0$ values lead to substantially higher values of $\mathcal{R}_{\rm ph}$ for Si XIII and S XV in WC01, Cassinelli et al. (2001), and Miller et al. (2002). This means that we would infer systematically larger radii than these authors, given the same measured value of $\mathcal{R}$.

Regardless of the differences between TLUSTY and Kurucz model atmospheres, there are substantial uncertainties in the Lyman flux of any model atmosphere; this part of the spectrum is generally inaccessible to observation, and the models' Lyman continua have not been directly verified experimentally. In the two cases in which early B stars have been directly observed in the Lyman continuum with the *Extreme Ultraviolet Explorer* (*EUVE*), the fluxes have been roughly an order of magnitude above model values (Cassinelli et al. 1995, 1996); however, it should be pointed out that these stars are significantly cooler than the O stars we are studying, so their Lyman fluxes are more sensitive to changes in the temperature structure in the outer atmosphere. Furthermore, the effective temperature scale used for O stars in the past may be systematically too high (Martins et al. 2002), which would also have more of an effect on the part of the spectrum shortward of the Lyman break. However, the effect of the uncertainty in the model Lyman continuum flux is significantly larger than the effect of the correction to the effective temperature scale.

2.4. *Helium-like Line Profiles*

Although it may sometimes be easier to measure the f/i ratio directly and compare it to a calculation for the ratio as a function of distance from the star, it is potentially much more powerful to calculate line profiles including the radial dependence of the line ratio and compare these to the data. The expression for the line profile derived in OC01 is

$$L_x = C \int_0^{u_x} du\, \frac{f_{\rm X}(u)}{w^3(u)} e^{-\tau(u,x)}, \tag{11}$$

where the volume filling factor of X-ray-emitting plasma is $f_{\rm X}(u) \propto u^q$, while x refers to the velocity-scaled dimensionless Doppler-shift parameter, and $\tau(u,x)$ is the optical depth along the line of sight to the observer, which is usually written as the product of a geometrical integral, $t(u,x)$, and a dimensionless constant, $\tau_* = \left(\kappa \dot{M}\right)/(4\pi v_\infty R_*)$, the characteristic optical depth. It should be noted that the expression for the optical depth is only analytic for integral values of the velocity-law index β; otherwise, it must be evaluated numerically. Because the expression for L_x must also be evaluated numerically, it is preferable to take

TABLE 3
COMPARISON OF He-LIKE RATIO CALCULATIONS

Star	Ion	Reference	$\overline{H_\nu/E}$[a]	P[b]	$\mathcal{R}_{\rm ph}/\mathcal{R}_0$	$\mathcal{R}_0$[c]	$\mathcal{R}_{\rm ph}$[d]
ζ Ori	Si XIII	This work	1.97	3.09	0.244	2.3	0.56
		WC01[e]	0.633	0.993	0.502	2.85	1.43
ζ Pup	S XV	This work	8.71	3.21	0.238	2.0	0.48
		C01[e]	4.95	1.82	0.355	2.04	0.72

NOTES.—In this table we compare the adopted photospheric UV flux and the helium-like triplet ratio calculations of WC01 and Cassinelli et al. (2001, C01) to those in this work.

[a] The photospheric UV flux, $\overline{H_\nu/E}$, is given in units of 10^7 photons cm^{-2} s^{-1} Hz^{-1}.

[b] $P \equiv \phi_*/\phi_c$ is discussed in eq. (3) and (4).

[c] For WC01 and C01 we used the $\mathcal{R}_0$ values shown on their plots.

[d] Our calculations for $\mathcal{R}_{\rm ph}$ (which is the value of $\mathcal{R}$ near the photosphere) using the Kurucz model atmospheres agree with the figures of WC01 and C01.

[e] We used Kurucz model atmospheres to reproduce these authors' calculations. We assumed that ζ Pup was represented by a model with $T_{\rm eff} = 40$ kK and $\log g = 4.0$ and ζ Ori by a model with $T_{\rm eff} = 30$ kK and $\log g = 3.5$.

β to be an integer in order to avoid a multidimensional integral. The best integer approximation for most O stars is $\beta = 1$ (see, e.g., Puls et al. [2006] for models that include clumping).

To account for the relative line strengths of the triplet, we simply multiply the integrand with the weighting factors $f(u) = G\mathcal{R}(u)/[1 + \mathcal{R}(u)]$ or $i(u) = G/[1 + \mathcal{R}(u)]$. This normalizes the forbidden and intercombination lines to the resonance line, which may be calculated using the above expression with no modification. If it is desirable to normalize the sum of all three weighting factors to unity, one may divide them by $1 + G$. In this work we have assumed that G does not vary with radius. Although G does depend on temperature, the variation is not strong, and the X-ray-emitting plasma is likely multiphase. If there is any variation in the line profile shapes caused by a radial dependence in G, it is not likely to be detectable except with data of very high statistical quality.

In comparison with the integrated plots presented in § 2.3, a line profile with $\tau_* > 0$ has a higher $\mathcal{R}$ ratio than one with no absorption, given the same value of u_0. This is because the forbidden line is only formed farther out where absorption is less, while the intercombination line is mainly formed close to the star, where absorption is greater. Nonzero positive values of q cause $\mathcal{R}$ to go down, because relatively more emission comes from close to the star, while negative values cause $\mathcal{R}$ to go up.

In comparison with normal line profiles, the intercombination line has weaker wings, as it becomes much weaker far away from the star. On the other hand, the forbidden line is relatively flat topped; because of photoexcitation, the profile appears as if it has a larger effective value of R_0 than the resonance line.

The addition of the radial dependence of the f/i ratio to the OC01 profile model has the appealing property of enforcing self-consistency between the radial dependences of the Doppler profile and the f/i ratio. In addition, although it does make the quite reasonable assumption that the X-ray-emitting plasma follows the same β-velocity law as the wind, it is not tied to any particular heating mechanism. In § 3, we use this model to fit *Chandra* HETGS spectra of four O stars.

3. DATA REDUCTION AND ANALYSIS

In this section we fit helium-like triplets in the *Chandra* HETGS data of four O stars: ζ Pup, ζ Ori, ι Ori, and δ Ori. We fit only Mg XI, Si XIII, and, for ζ Pup, S XV. This is because Ne IX and lower Z helium-like species generally have $\mathcal{R} < 0.2$ in O stars and therefore do not contain significant information in the line ratio.

3.1. *Data Processing*

Primary data products were obtained from the *Chandra* data archive and processed using standard CIAO routines outlined in the CIAO grating spectroscopy threads.[3] The versions used were CIAO 3.1 and CALDB 2.28. The spectral fitting was done with XSPEC 11.3.1. The *C*-statistic (Cash 1979) is used instead of χ^2 because of the low number of counts per bin. For ζ Ori and ι Ori the data were split into two observations each, which were fit simultaneously. Emission lines were fit over a wavelength range of $[\lambda_r(1 - v_\infty/c) - \Delta\lambda,\ \lambda_f(1 + v_\infty/c) + \Delta\lambda]$, where $\Delta\lambda$ is the resolution of MEG at that wavelength. This range was chosen to include the entire emission line but at the same time to prevent the quality of the continuum fit from influencing the fit statistic for the line. To get the continuum strength for a given line, we first fit it outside this range, but near the wavelength of the line.

[3] See http://cxc.harvard.edu/ciao/threads/gspec.html.

Because the MEG has substantially more effective area than the HEG at longer wavelengths, we used only the MEG ±1 order data for Si XIII in ζ Pup and for Mg XI for all stars. For the S XV complex in ζ Pup and the Si XIII complex in the other stars, the statistics are poorer, and the contribution of the HEG is significant, so we simultaneously fit both the HEG and MEG ±1 order data. The MEG ±1 order data for Si XIII in ζ Ori are inconsistent, so we fit each of them separately; this inconsistency is discussed in more detail in § 4.

3.2. *Fitting Procedure*

We use two different fitting procedures, depending on the number of counts in the triplet. For triplets with many counts (Mg XI for all stars and Si XIII for ζ Pup), we fit them with the helium-like OC01 profile described in § 2.4. The fixed model parameters are the line rest wavelengths, the terminal velocity of the wind, the velocity-law index $\beta = 1$, the unaltered f/i ratio $\mathcal{R}_0$, and the averaged photospheric UV strength. The fit parameters from the profile model are q, τ_*, and u_0, in addition to the G ratio and the overall normalization. The four fit parameters other than normalization are fit on a grid with spacing 0.2 for q and τ_*, and spacing 0.05 for u_0 and G.

For lines with few counts (S XV for ζ Pup and Si XIII for the other stars), we fit a three-Gaussian model to prevent overinterpretation. Rather than using three individual Gaussians, which would have three separate normalizations, we use a model with parameters G, $\mathcal{R}$, the overall normalization, and the velocity width, which is taken to be the same for all the lines in a given complex. This avoids fitting problems due to covariance in individual line normalizations, which can be a problem in blended line complexes. It also allows us to directly measure the line ratios and their errors, which are the quantities of interest. We fit the parameters on a grid with spacing 2×10^{-3} for σ_v, 0.2 for $\mathcal{R}$, and 0.1 or 0.2 for G. We interpret the results of these multi-Gaussian fits using the integrated ratio formalism described in § 2.3 and shown in Figures 3–6.

In all cases we add a continuum component to approximate bremsstrahlung emission. This is represented by a power law of index 2 with normalization chosen to fit the continuum near the line. Care is taken to avoid including moderately weak spectral lines in the continuum fit. A power law of index 2 is not necessarily appropriate for the continuum in general, but over a sufficiently short range in wavelength, any reasonable continuum shape is statistically indistinguishable. An index of 2 is chosen because this gives a flat continuum when F_λ is plotted versus wavelength.

We do not expect any other strong lines to contaminate our line fits. Mg XII Lyγ is at approximately the same wavelength as the Si XIII forbidden line, but even in ζ Ori, where Si XIII is relatively weak, the strength of Mg XII Lyγ expected based on the strength of Mg XII Lyα is not enough to affect our measurements significantly.

4. RESULTS

The results of the fits are summarized in Tables 4 and 5. The fits are plotted with the data in Figures 7–21. The data have been rebinned for presentation purposes in some of the plots, but in all cases the data were fit without rebinning.

We show two-parameter confidence interval plots for the profile fit to Mg XI for ζ Pup in Figure 22. These confidence intervals are qualitatively representative of our results for all the line complexes; they demonstrate that there is a moderate correlation of the parameters q and u_0 in the profile fits and that the other

TABLE 4
PARAMETERS FOR He-like PROFILE FITS

Star	Ion	q	τ_*	u_0	R_0[a]	G	$\mathcal{R}$[b]	Flux[c]	C	Bins	MC[d]
ζ Pup	Mg XI	$0.0^{+0.4}_{-0.2}$	1.0 ± 0.4	0.70 ± 0.05	1.43	$0.70^{+0.15}_{-0.10}$	0.41	17.7 ± 0.9	135.3	136	39.1
	Si XIII	$0.0^{+0.6}_{-0.4}$	$0.6^{+0.4}_{-0.2}$	$0.70^{+0.05}_{-0.10}$	1.43	1.05 ± 0.15	0.90	11.9 ± 0.7	116.2	98	84.7
ζ Ori	Mg XI	$-0.4^{+1.0}_{-0.2}$	0.2 ± 0.2	$0.6^{+0.10}_{-0.1*}$	1.67	$1.05^{+0.05*}_{-0.2}$	0.82	$6.5^{+0.5}_{-0.6}$	267.2	240	73.4
ι Ori	Mg XI	$-0.8^{+0.2}_{-0.0}$	$0.0^{+0.2}_{-0.0}$	$0.75^{+0.05}_{-0.10}$	1.33	$0.90^{+0.20*}_{-0.25}$	0.72	3.5 ± 0.5	266.6	256	80.2
δ Ori	Mg XI	$-0.8^{+0.4}_{-0.0}$	$0.0^{+0.2}_{-0.0}$	$0.80^{+0.05}_{-0.10}$	1.25	$0.60^{+0.25}_{-0.10*}$	0.75	4.0 ± 0.5	123.9	124	18.2

NOTES.—Errors are 2 σ, or $\Delta C = 4$ for 1 degree of freedom. Asterisks indicate parameters that were still within 2 σ at the edge of the fit range.
[a] R_0 is given in units of the stellar radius; it is calculated from $R_0 = 1/u_0$, and retains an extra digit to avoid rounding error.
[b] $\mathcal{R}$ is reported without an uncertainty, because it is the value of the f/i ratio calculated by the best-fit model.
[c] Flux is given in units of 10^{-5} photons cm^{-2} s^{-1}.
[d] MC is the percentage of Monte Carlo realizations of the model having C less than the data does for that model.

parameters are not strongly correlated. The correlation in q and u_0 is expected, as both parameters influence the radial distribution of plasma and, therefore, both the f/i ratio and the profile width.

The goodness of fit is tested by comparing the fit statistic to that obtained from Monte Carlo simulations from the model. The percentage of 1000 realizations having C less than the data is given in the tables of results. These percentages can be thought of as rejection probabilities.

The helium-like line profile fits generally are adequate to explain the data; they are all formally statistically acceptable. The fact that the fits can simultaneously account for the profile shape and the f/i ratio indicates that the values of u_0 obtained are not an artifact of the profile model. In other words, we can explain both the line ratios and profile shapes with a single model for the radial distribution of X-ray-emitting plasma.

The fit parameters obtained for the helium-like profile fits are generally consistent with those obtained in Kramer et al. (2003) and Cohen et al. (2006) from non–helium-like line profile fits. The $\mathcal{R}$ ratios for the helium-like line profile fits are also consistent with those measured in Kahn et al. (2001), WC01, Cassinelli et al. (2001), and Miller et al. (2002). The values of u_0 for all four stars fall in the range $0.6 < u_0 < 0.8$, or $1.25 < R_0 < 1.67$. This is substantially closer to the star than the values of u inferred in Kahn et al. (2001), WC01, and Cassinelli et al. (2001) from f/i ratios. This reflects the difference between assuming a single radius of formation as opposed to a distribution of radii.

We now consider the lower signal-to-noise ratio complexes, which we fit with Gaussians. For the Si XIII lines in ι Ori and δ Ori, the $\mathcal{R}$ ratio is not strongly constrained, and in both cases the data are consistent with $\mathcal{R} = \mathcal{R}_0$. The goodness of fit is formally acceptable in both cases. If anything, it is surprising that the $\mathcal{R}$ ratio is not slightly lower in both cases, considering the values of u_0 measured for the Mg XI lines.

The $\mathcal{R}$ ratio measured in S XV in ζ Pup is equivalent to a value of $R_0 = 1.1^{+0.4}_{-0.1}$, based on Figure 3. The 1 σ upper limit to R_0 is consistent with what is seen in other lines and with the expectations of hydrodynamic models of wind shocks (Feldmeier et al. 1997b; Runacres & Owocki 2002). The fit to these lines is formally acceptable.

The fit to the Si XIII complex of ζ Ori is poor. Because the positive and negative first-order MEG data look very different, we fit them separately, in addition to the joint fit. These additional fits are shown in Figures 13 and 14. Part of the difference in appearance is a result of the Si XIII complex falling on a chip gap in the negative first-order, which reduces the effective area and makes it uneven. However, even accounting for this, there is a substantial difference in the fit results for the two orders, both for $\mathcal{R}$ and for G. It is possible to get a satisfactory fit using only the positive first-order MEG data, but fitting the negative first order by itself gives a poor fit. Because the negative first-order data for this complex falls on a chip gap, cannot be fit well by a three-Gaussian model, and has substantially fewer counts than the positive first order, we consider it to be unreliable.

In Table 6 we compare our fits for Si XIII in ζ Ori and S XV in ζ Pup to those of WC01 and Cassinelli et al. (2001), respectively. There is not enough information in their original work to directly compare their best-fit model to ours; they do not give the velocity broadenings or overall normalizations. We use their published values of $\mathcal{R}$ and G and find the best-fit parameters for velocity

TABLE 5
PARAMETERS FOR HELIUM-LIKE GAUSSIAN FITS

Star	Ion	σ_v/c (10^{-3})	$\mathcal{R}$	G	Flux[a]	C	Bins	MC[b]	R_0
ζ Pup	S XV	2.4 ± 0.4	1.0 ± 0.4	0.9 ± 0.2	3.1 ± 0.3	191.2	216	78.4	$1.1^{+0.4}_{-0.1}$
ζ Ori	Si XIII[c]	$2.4^{+0.2}_{-0.0}$	2.8 ± 0.8	$1.2^{+0.2}_{-0.1}$	2.45 ± 0.15	432.1	496	97.9	≥ 2.1
	Si XIII[d]	2.0 ± 0.2	≥ 2.8	0.9 ± 0.2	2.4 ± 0.4	57.6	59	35.3	∞
	Si XIII[e]	$3.0^{+0.8}_{-0.6}$	≥ 1.6	$2.0^{+1.0*}_{-0.6}$	$2.4^{+0.6}_{-0.5}$	85.6	59	98.8	≥ 1.4
ι Ori	Si XIII	2.8 ± 0.4	$2.8^{+0.6}_{-0.8}$	$1.6^{+0.4}_{-0.2}$	1.54 ± 0.24	305.1	532	84.9	≥ 3.2
δ Ori	Si XIII	$1.2^{+0.0}_{-0.2}$	$2.2^{+1.0}_{-0.4}$	0.7 ± 0.1	1.88 ± 0.16	214.0	258	62.9	≥ 2.2

NOTES.—Errors are 1 σ, or $\Delta C = 1$. Asterisks indicate parameters that were still within 1 σ at the edge of the fit range.
[a] Flux is in units of 10^{-5} photons cm^{-2} s^{-1}.
[b] MC is the percentage of Monte Carlo realizations of the model having C less than the data does for that model.
[c] Combined fit to positive and negative first-order HEG and MEG data.
[d] Fit to positive first-order MEG data only.
[e] Fit to negative first-order MEG data only.

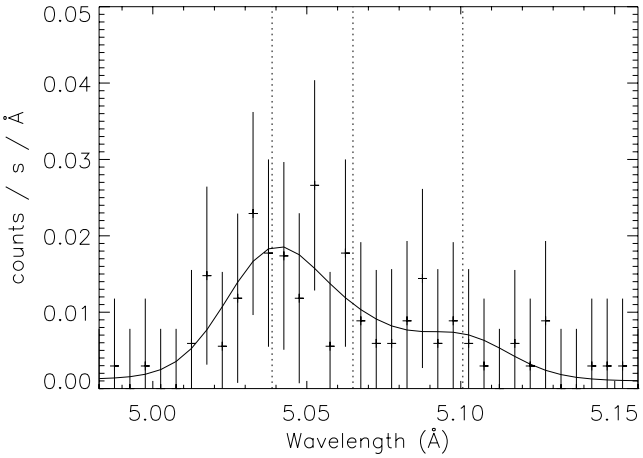

FIG. 7.—MEG data and best-fit model for S XV in ζ Pup. The positive and negative first-order data have been co-added. The data are shown with error bars, and the model is shown as a solid line. The rest wavelengths of the resonance, intercombination, and forbidden lines are shown with dotted lines. In the subsequent figures, except where stated explicitly, the plots of Gaussian fits show the joint best fit to both the HEG and MEG data, even though data from only one grating are presented at a time.

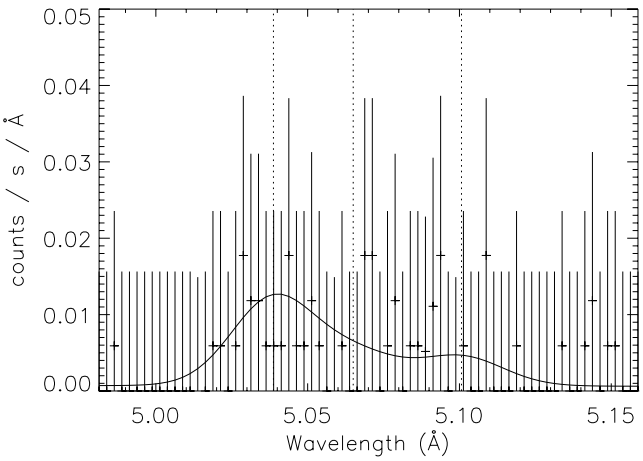

FIG. 8.—Same as Fig. 7, but for HEG data and best-fit model for S XV in ζ Pup.

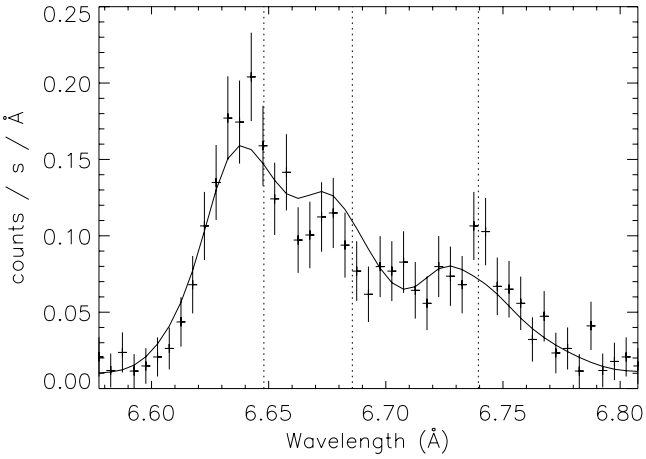

FIG. 9.—Same as Fig. 7, but for MEG data and best-fit model for Si XIII in ζ Pup.

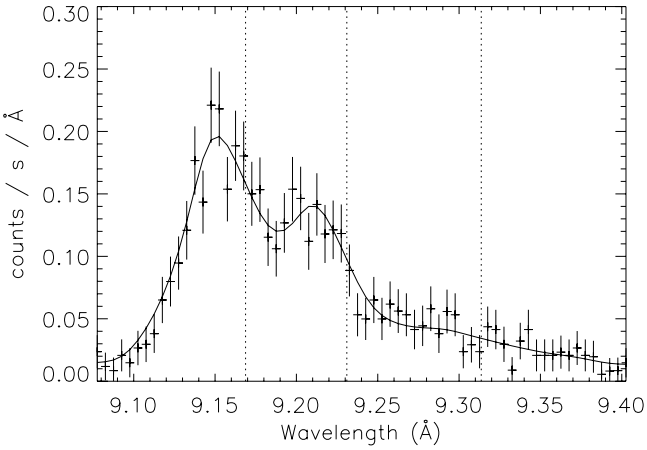

FIG. 10.—Same as Fig. 7, but for MEG data and best-fit model for Mg XI in ζ Pup.

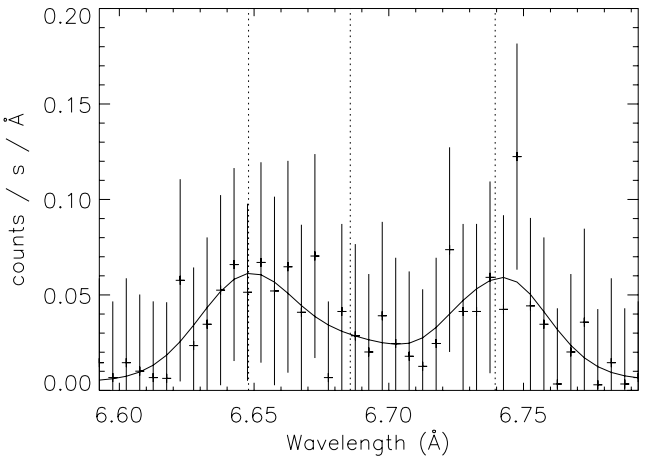

FIG. 11.—Same as Fig. 7, but for MEG data and best-fit model for Si XIII in ζ Ori. Figs. 13 and 14 show the positive and negative first-order MEG data separately.

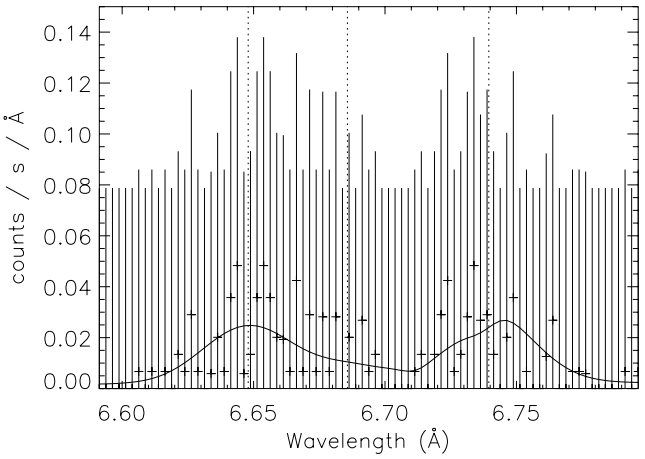

FIG. 12.—Same as Fig. 7, but for HEG data and best-fit model for Si XIII in ζ Ori.

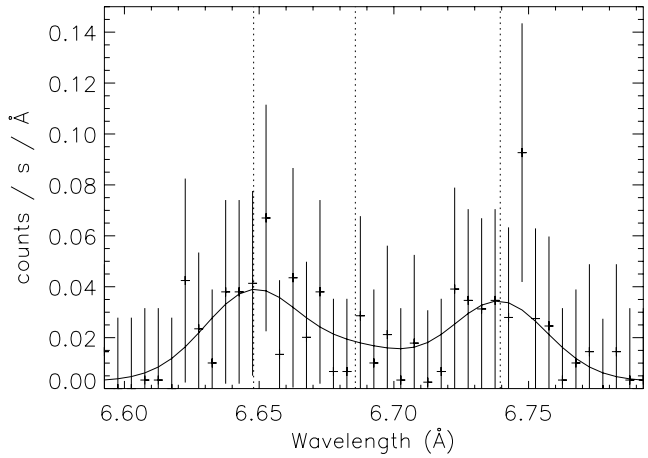

FIG. 13.—Same as Fig. 7, but for MEG positive first-order data and best-fit model for Si XIII in ζ Ori. The model is the best fit to only the *positive* first-order data.

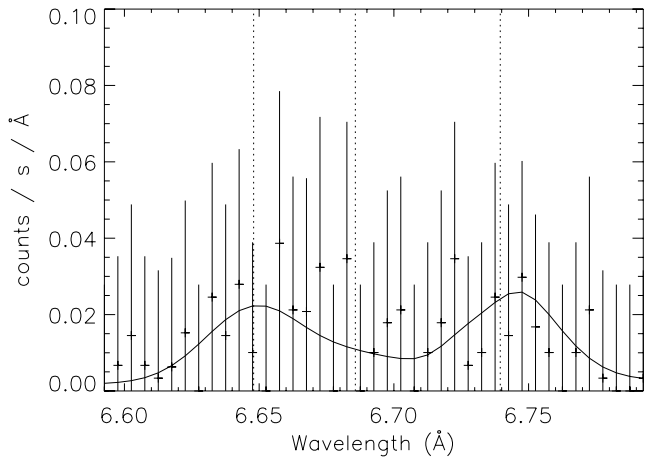

FIG. 14.—Same as Fig. 7, but for MEG negative first-order data and best-fit model for Si XIII in ζ Ori. The model is the best fit to only the *negative* first-order data.

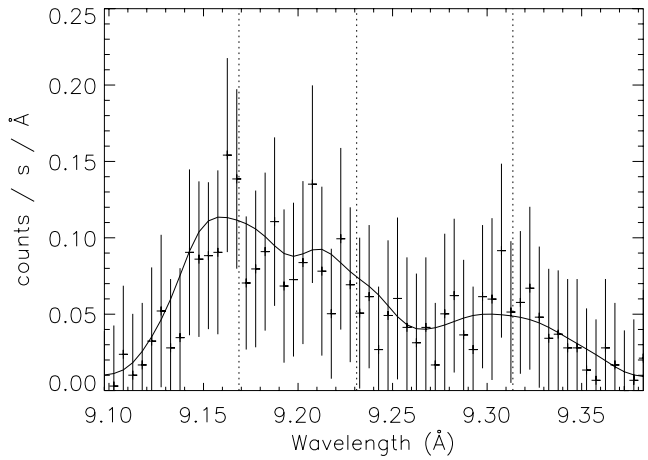

FIG. 15.—Same as Fig. 7, but for MEG data and best-fit model for Mg XI in ζ Ori.

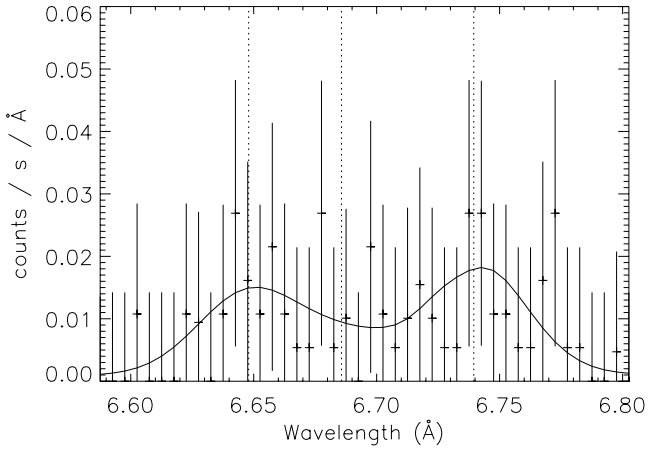

FIG. 16.—Same as Fig. 7, but for MEG data and best-fit model for Si XIII in ι Ori.

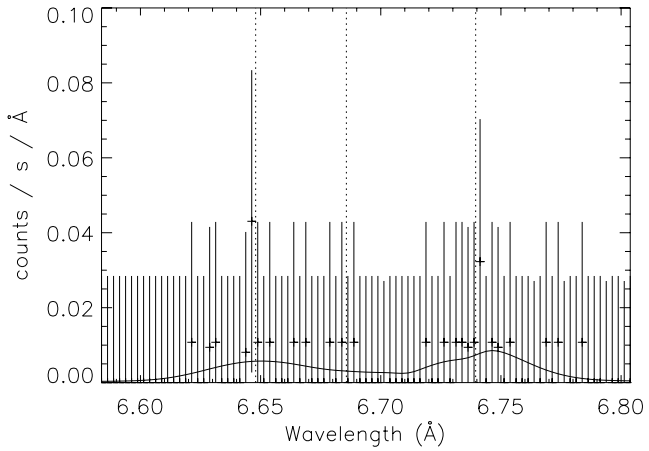

FIG. 17.—Same as Fig. 7, but for HEG data and best-fit model for Si XIII in ι Ori.

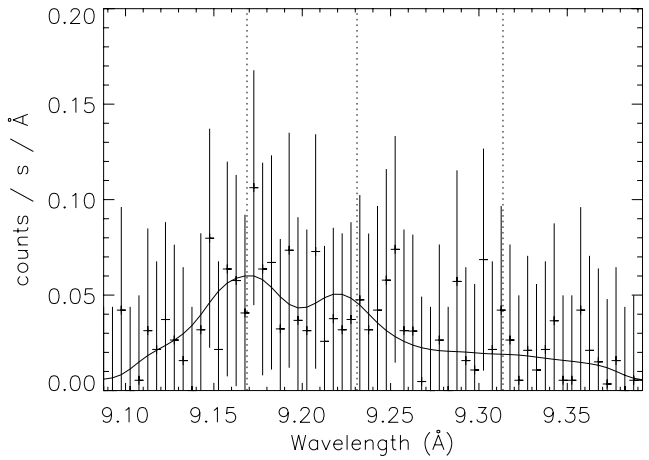

FIG. 18.—Same as Fig. 7, but for MEG data and best-fit model for Mg XI in ι Ori.

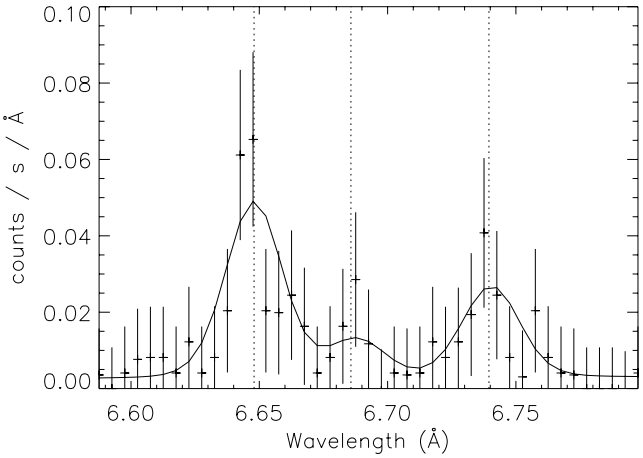

FIG. 19.—Same as Fig. 7, but for MEG data and best-fit model for Si XIII in δ Ori.

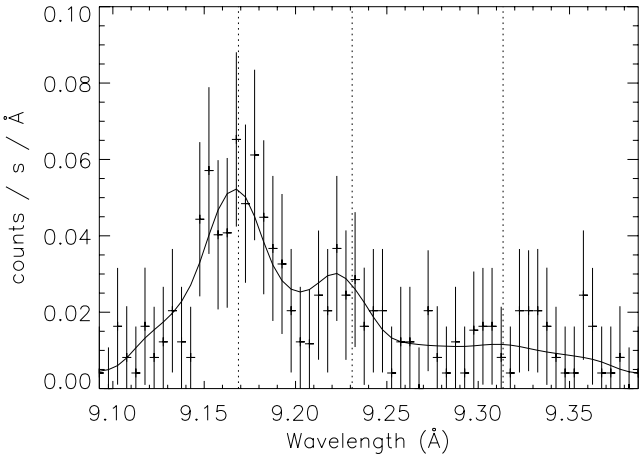

FIG. 21.—Same as Fig. 7, but for MEG data and best-fit model for Mg XI in δ Ori.

broadening and normalization. WC01 do not present their measurements of G, but we infer from the temperature range they claim is allowed that they measure G in the range 0.8–2.0. We assume the best fit was in the middle of this range, or $G = 1.4$. In both cases we also tried letting G be a free parameter, in order to test the validity of their $\mathcal{R}$ measurements independently of any claims about G. For S XV in ζ Pup, we found that the best fit occurs with a substantially different value of G than that reported by Cassinelli et al. (2001).

Our measurement of the $\mathcal{R}$ ratio of Si XIII in ζ Ori is significantly different than that of WC01. Statistically, their best-fit measurement has a C value that is 11.7 greater than our best fit. For one interesting parameter, this is excluded at more than 3 σ. The reported value of $\mathcal{R} = 1.2 \pm 0.5$ is also very different than our measured value of 2.8 ± 0.8. Two points should be reiterated. First, when fitting all the data we do not get a statistically acceptable fit, but the positive first-order MEG data can be well fit, and this fit has an $\mathcal{R}$ ratio that is comparable to the value we measure using all the data. Furthermore, whether we use all the data or exclude the questionable negative first-order MEG data from the fit, we get essentially the same result. Second, we are using essentially the same model as WC01 but merely measure very different parameter values, even when fitting exactly the same data. This may stem from the fact that WC01 used very early versions of the CIAO tools (J. P. Cassinelli 2006, private communication).

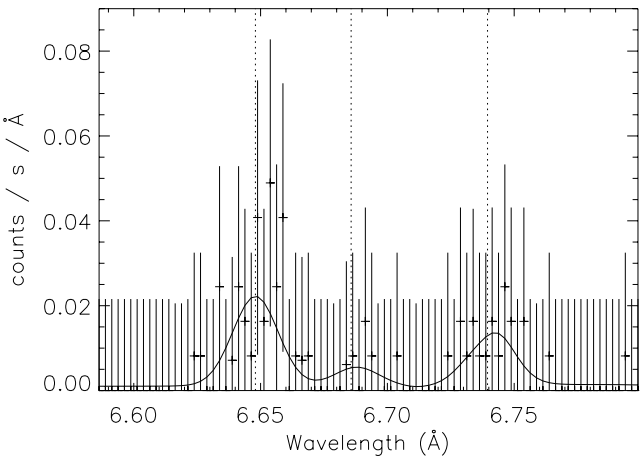

FIG. 20.—Same as Fig. 7, but for HEG data and best-fit model for Si XIII in δ Ori.

Our measurement of the $\mathcal{R}$ ratio of S XV in ζ Pup is somewhat different than that of Cassinelli et al. (2001). We also found that the if we fix $\mathcal{R}$ to the value they reported, the best-fit value of G is substantially different than their measurement. Although their best-fit model with $\mathcal{R} = 0.61$ is not excluded at the 1 σ level, the model based on their measured value of G has a value of C that is greater than that of our best fit by 9.5, despite the fact that we both fit a three-Gaussian model. Although we do not exclude their best-fit value of $\mathcal{R}$ at 1 σ, it is also puzzling that our range of fit values should be significantly different from that of the previous work.

5. DISCUSSION

We have used the f/i ratios of helium-like triplets in conjunction with their line profiles to constrain the radial distribution of X-ray-emitting plasma in O stars. Our results are consistent with the results of Kramer et al. (2003) and Cohen et al. (2006) in the sense that the spatial distribution we infer from f/i ratios (additionally constrained in some cases by line profile fitting) is consistent with these authors' results from fitting line profiles to individual lines with high signal-to-noise ratios.

Our results for Si XIII in ζ Ori are different from the initial analysis, which claimed that the location of the emitting plasma was extremely close to the star. These differences are due both to our assessment of the relative line fluxes and to our modeling of the line formation. Table 6 shows a comparison of our measurements and inferred radii of formation; we find that the Si XIII is at least 1.1 stellar radii above the photosphere ($R_0/R_* = 2.1$). Part of the difference in inferred radii originates in our different calculations of the radial dependence of $\mathcal{R}$. This is illustrated in Figure 23, where we plot our calculations and measurements of $\overline{\mathcal{R}}(u_0)$ and compare them to the calculations and measurements of $\mathcal{R}(u)$ from WC01. (It is important to note that the range of radii indicated on the plot by the thickened lines refers to that allowed by the statistical error in the measurement of $\mathcal{R}$ and not to a physical extent of the X-ray-emitting plasma.) We also show what our inferred radius of formation would be if we inferred a single radius from our measured value of $\mathcal{R}$ instead of an onset radius R_0 in a distributed model (assuming that an averaged value of the photospheric UV flux could be used). This is intended to make it clear that the major sources of disagreement are the actual $\mathcal{R}$ measurements and the UV fluxes of the adopted model atmospheres. In fact, even taking the reported upper limit on $\mathcal{R}$ (of 1.7) from WC01 and assuming a single radius of formation (Fig. 23, *dash-dotted curve*), our analysis shows that the formation

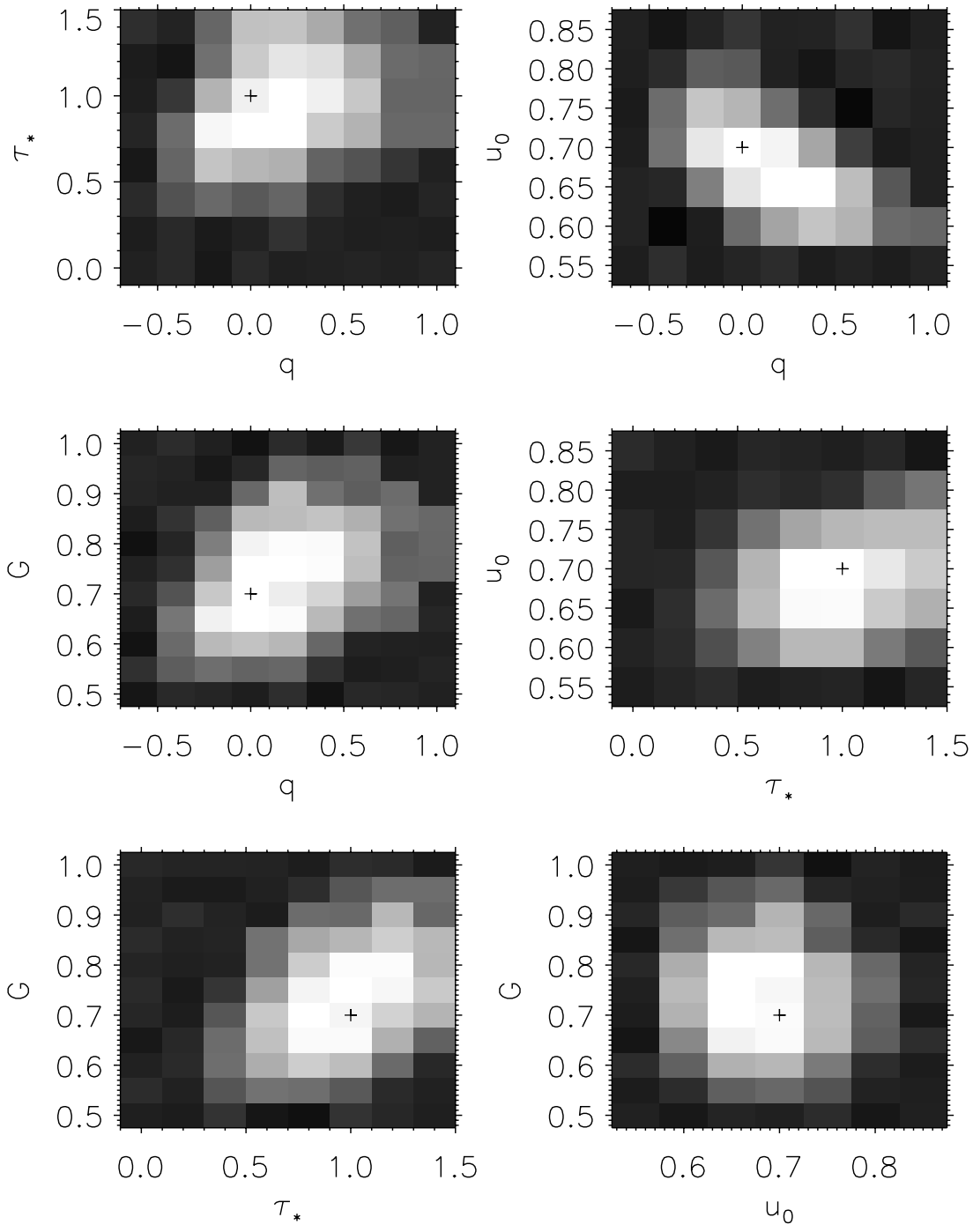

FIG. 22.—Two-dimensional plots of confidence intervals for fit parameters for Mg XI in ζ Pup. The shades of gray represent 1, 2, and 3 σ, or $\Delta C < 2.3$, 6.17, and 11.8 (as appropriate for 2 degrees of freedom), and the plus sign represents the best fit. There is a moderate correlation of the fit parameters q and u_0, as one would expect. We have made similar plots for the other helium-like profile fits (not shown) to look for correlations in fit parameters. These plots also show a moderate correlation between q and u_0.

radius is consistent with values larger than $2R_*$. Although we also assume a spatial distribution of X-ray-emitting plasma, this does not contribute to the new, larger formation radii.

We make a similar comparison with the earlier results (Cassinelli et al. 2001) for S XV for ζ Pup in Table 6 and Figure 24. In this case the measured range of allowed values of $\mathcal{R}$ is different but overlapping. The different measured range of $\mathcal{R}$ combined with a somewhat higher model photospheric UV flux leads us to infer a minimum radius of formation as large as $1.5R_*$; however, the allowed range of minimum radii extends down to nearly the photosphere, in agreement with the results of Cassinelli et al. (2001). The upper range of allowed minimum radii is reasonable in the context of stellar wind models for X-ray-emitting plasma formation, but the lower range is certainly not. While the difference between our measurements and calculations and those of Cassinelli et al. (2001) is not great, it is enough to allow the possibility that the S XV emission could reasonably be produced in a wind-shock model.

These results obviate the need for any kind of two-component model for the origin of X-ray emission in O stars, as suggested by WC01, Cassinelli et al. (2001), and Mullan & Waldron (2006). For the Si XIII line in ζ Ori, the range of acceptable minimum radii

TABLE 6
Comparison of Fit Parameters

Star	Ion	Reference	σ_v/c (10^{-3})	$\mathcal{R}$	G	C	Bins	R_0, R[a]
ζ Pup	S XV	This work	2.4	1.0	0.9	191.2	216	$1.1^{+0.4}_{-0.1}$
		C01a[b]	2.8	0.61	2.06	200.7		<1.2
		C01b[c]	2.4	0.61	0.9	192.0		...
ζ Ori	Si XIII	This work	2.4	2.8	1.2	432.1	496	≥ 2.1
		WC01[d]	2.2	1.2	1.4	443.8		<1.08

Notes.—In this table we compare our fit parameters to those of Cassinelli et al. (2001, C01) and WC01 for two line complexes. In all cases we used the best-fit σ_v and normalization.

[a] For our work this column gives the inferred minimum radius of formation R_0, while for the previous work this column gives the inferred radius of formation R.

[b] For C01a we used the published value of $\mathcal{R}$ and G.

[c] For C01b we used the published value of $\mathcal{R}$ and the best-fit value for G.

[d] For WC01 the published value of G was the best fit, assuming their value of $\mathcal{R}$.

of formation we infer is quite reasonable in the wind-shock paradigm. For the S XV line in ζ Pup, the upper end of the range of acceptable minimum radii of formation we infer is acceptable in the wind-shock paradigm, although the lower end of the range is not. Taken together, we can say that the wind-shock paradigm is consistent with these data; we do not exclude the possibility that S XV in ζ Pup is formed very close to the star or is formed in a process outside of the wind-shock paradigm, but we do not require this. We note that numerical simulations of the line-driven instability show that large shock velocities, and therefore hot plasma, occur quite deep in the wind, almost as soon as the damping effects of the diffuse radiation field are overcome by the onset of the instability growth (Runacres & Owocki 2002). While hybrid wind-coronal mechanisms are not excluded by the data, there is nothing in the X-ray spectral data that requires such complex models, and the principle of Occam's razor leads us to suggest that it is more reasonable to assume a wind shock origin for all X-rays from the O stars we are studying, if it is possible to explain the data this way. Another argument against inferring extremely small formation radii for these two ions is the lack of any evidence, either from line profiles or from f/i ratios, of the presence of emission from lower ion stages at these very small radii, as would be expected from the rapid radiative cooling of plasma containing S XV or Si XIII at the densities expected this far down in the wind.

It should be noted that there is one other claim in the literature of an anomalously low f/i ratio measurement requiring an X-ray production mechanism outside of the standard wind-shock paradigm. Waldron et al. (2004) find evidence for this in their analysis of the X-ray spectrum of Cyg OB2 8A (VI Cyg 8A); in this case the basis for their claim is emission from S XV and Ar XVII. However, these ions' $2\,^3S_1 \rightarrow 2\,^3P_J$ transitions are in the Lyman continuum, where results are very sensitive to model atmosphere uncertainties, so the inferred radii are subject to substantial uncertainties. Furthermore, the data have very low signal-to-noise ratios.

The characteristic optical depths we measure from profile fits are substantially smaller than one would expect, given the published mass-loss rates. Detailed calculations of the expected values of τ_* are beyond the scope of this paper, but it is safe to say that we would expect to see characteristic optical depths at least of order a few at 9 Å; our measurements for Mg XI give $\tau_* = 1$ for ζ Pup and less for the other stars. However, Si XIII and Mg XI give poorer constraints on the optical-depth/mass-loss-rate discrepancy

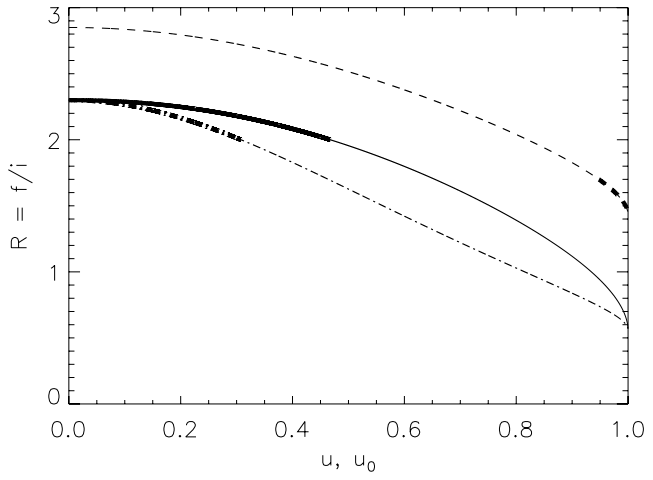

Fig. 23.—Comparison of measurements and calculations for Si XIII in ζ Ori. Calculations are thin lines, and measurements are thickened over the allowed range of $\mathcal{R}$. The solid line shows $\overline{\mathcal{R}}(u_0)$ from this work; the dash-dot line shows the $\mathcal{R}(u)$ for a single radius, but using an averaged value of the TLUSTY UV flux; and the dashed line shows the calculations and measurements of WC01. Note that the range shown by the thickened lines represents the allowed range of measured $\mathcal{R}$ or $\overline{\mathcal{R}}$ values, and does not represent the physical extent of the X-ray-emitting plasma. In the case of $\mathcal{R}$, the model assumes a single radius of formation, while for $\overline{\mathcal{R}}$ the value of u_0 inferred corresponds to the minimum radius for X-ray emission. The fact that the allowed range of $\mathcal{R}$ graphically mimics the distribution of plasma radii for the upper limit value to u_0 is a coincidence.

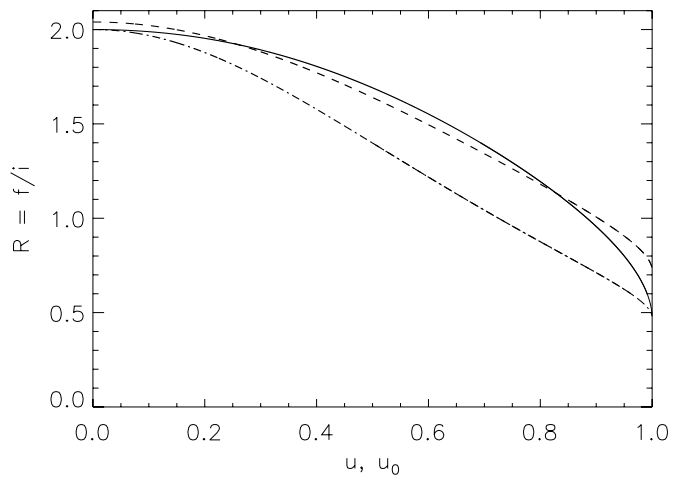

Fig. 24.—Same as Fig. 23, but for S XV for ζ Pup, and the dashed line shows the calculations and measurements of Cassinelli et al. (2001).

TABLE 7
Comparison of R_1 to R_0

Star	Ion	R_1	R_0[a]
ζ Pup	Mg XI	2.5	1.43 ± 0.10
	Ne IX	5	<2.5
	O VII	4	<4
ζ Ori	Mg XI	1.5	$1.67^{+0.33}_{-0.24}$
	Ne IX	2.8	<2.22
	O VII	2.2	<2.85
δ Ori	Mg XI	1.2	$1.25^{+0.18}_{-0.07}$
	Ne IX	2.1	<2.22
	O VII	2.8	<3.33

Notes.—In this table we compare the radius of optical depth unity R_1 calculated by WC01, Cassinelli et al. (2001), and Miller et al. (2002) to measurements of R_0, the minimum onset radius for X-ray emission.

[a] R_0 is measured using an helium-like line profile fit for Mg XI (see Table 4). Upper limits for O VII and Ne IX are derived from upper limits to the f/i ratio of $\mathcal{R} < 0.1$ and <0.2, respectively, which are taken to be representative for all three stars.

than longer wavelength lines, such as O VIII and N VII Lyα, where the photoelectric absorption cross section per unit mass is higher, so τ_* is larger and produces a more asymmetric profile.

WC01, Cassinelli et al. (2001), and Miller et al. (2002) compare the radii they infer from measurements of f/i ratios in helium-like triplets to the radii of optical depth unity, R_1, for the wavelength at which that helium-like ion emits. These values of R_1 were calculated using mass-loss rates from the literature and assumed a smooth wind density. They claim that the inferred radii correspond roughly to R_1, so that we are observing plasma at the closest point to the star where we can see it. Kahn et al. (2001) make a similar conjecture. Table 7 compares the values of R_1 from these papers to those derived using the methodology of this paper. Several lines show evidence for emission from inside the predicted R_1. This is in agreement with the low values of τ_* we have measured, as well as the measurements of Kramer et al. (2003) and Cohen et al. (2006). There is now mounting evidence from analysis of unsaturated UV line profiles that the literature mass-loss rates of O stars may be too high by at least a factor of a few (Massa et al. 2003; Hillier et al. 2003; Bouret et al. 2005; Fullerton et al. 2006). In addition, porosity may reduce the effective X-ray optical depths of O-star winds (Feldmeier et al. 2003; Oskinova et al. 2004, 2006; Owocki & Cohen 2006).

6. CONCLUSIONS

We have investigated the effect of a radially distributed plasma on the forbidden-to-intercombination line ratio in helium-like triplets, as well as variations in the exciting photospheric flux as a function of Doppler shift throughout the wind. We find that the fact that the plasma is likely distributed over a range of radii and Doppler shifts allows us to use an averaged value of the photospheric continuum instead of accounting for it in detail. We also find that the value of R_0 derived assuming a distribution of radii is substantially smaller than the value of R derived assuming a single radius.

We have used the f/i ratio of helium-like triplets to constrain the radial distribution of X-ray-emitting plasma in four O-type stars. We find that the minimum radius of emission is typically $0.6 < u_0 < 0.8$, or $1.25 < R_0/R_* < 1.67$, with the emission extending beyond this initial radius with either a constant filling factor or one that increases slightly with radius. This is consistent with the results of line-profile fits using the model of OC01 (Kramer et al. 2003; Cohen et al. 2006). However, some of the minimum radii of formation are well inside the radius of optical depth unity calculated using the mass-loss rates in the literature, implying that either the effective opacities are lower (e.g., due to porosity effects; Feldmeier et al. 2003; Oskinova et al. 2004, 2006; Owocki & Cohen 2006) or the mass-loss rates are lower than the literature values (Massa et al. 2003; Hillier et al. 2003; Bouret et al. 2005; Fullerton et al. 2006), or both. We also measure low values of the characteristic optical depth τ_* compared to what one would expect based on the literature mass-loss rates, which is consistent with the same conclusions.

We find that there is no evidence for anomalously low f/i ratios in high-Z species. Our measurements do not require X-ray emission to originate too close to the star to have sufficiently strong shocks, nor do we need to posit the existence of a magnetically confined corona. This conclusion is based partly on different measured values of f/i ratios and partly on higher photospheric UV fluxes on the blue side of the Lyman edge in the more recent TLUSTY model spectra.

We have fit helium-like emission line complexes with profile models that simultaneously account for profile shapes and line ratios. These models constrain the radial distribution of plasma both through the line ratio and the profile parameters u_0 and q. We find that they are capable of producing good fits to the data, showing that the information contained in the line ratios and profile shapes are mutually consistent.

We thank J. Cassinelli and the anonymous referee for many useful comments that led to improvements in the manuscript. M. A. L. acknowledges NASA grant NNG 04-GL76G. D. H. C. acknowledges NASA contract AR5-6003X to Swarthmore College through the *Chandra* X-ray Center.

REFERENCES

Blumenthal, G. R., Drake, G. W. F., & Tucker, W. H. 1972, ApJ, 172, 205 (BDT72)
Bouret, J.-C., Lanz, T., & Hillier, D. J. 2005, A&A, 438, 301
Cash, W. 1979, ApJ, 228, 939
Cassinelli, J. P., Miller, N. A., Waldron, W. L., MacFarlane, J. J., & Cohen, D. H. 2001, ApJ, 554, L55
Cassinelli, J. P., & Olson, G. L. 1979, ApJ, 229, 304
Cassinelli, J. P., & Swank, J. H. 1983, ApJ, 271, 681
Cassinelli, J. P., et al. 1995, ApJ, 438, 932
———. 1996, ApJ, 460, 949
Charbonneau, P., & MacGregor, K. B. 2001, ApJ, 559, 1094
Cohen, D. H., de Messières, G. E., MacFarlane, J. J., Miller, N. A., Cassinelli, J. P., Owocki, S. P., & Liedahl, D. A. 2003, ApJ, 586, 495
Cohen, D. H., Leutenegger, M. A., Grizzard, K. T., Reed, C. L., Kramer, R. H., & Owocki, S. P. 2006, MNRAS, 368, 1905
Crowther, P. A., Hillier, D. J., Evans, C. J., Fullerton, A. W., De Marco, O., & Willis, A. J. 2002, ApJ, 579, 774
Dere, K. P., Landi, E., Mason, H. E., Monsignori Fossi, B. C., & Young, P. R. 1997, A&AS, 125, 149
Donati, J.-F., Babel, J., Harries, T. J., Howarth, I. D., Petit, P., & Semel, M. 2002, MNRAS, 333, 55
Donati, J.-F., et al. 2006, MNRAS, 370, 629
Feldmeier, A. 1995, A&A, 299, 523
Feldmeier, A., Kudritzki, R.-P., Palsa, R., Pauldrach, A. W. A., & Puls, J. 1997a, A&A, 320, 899
Feldmeier, A., Oskinova, L., & Hamann, W.-R. 2003, A&A, 403, 217
Feldmeier, A., Puls, J., & Pauldrach, A. W. A. 1997b, A&A, 322, 878
Fullerton, A. W., Massa, D. L., & Prinja, R. K. 2006, ApJ, 637, 1025
Gabriel, A. H., & Jordan, C. 1969, MNRAS, 145, 241 (GJ69)
———. 1973, ApJ, 186, 327

Gagné, M., Oksala, M. E., Cohen, D. H., Tonnesen, S. K., ud-Doula, A., Owocki, S. P., Townsend, R. H. D., & MacFarlane, J. J. 2005, ApJ, 628, 986
Harnden, F. R., et al. 1979, ApJ, 234, L51
Hillier, D. J., Kudritzki, R. P., Pauldrach, A. W., Baade, D., Cassinelli, J. P., Puls, J., & Schmitt, J. H. M. M. 1993, A&A, 276, 117
Hillier, D. J., Lanz, T., Heap, S. R., Hubeny, I., Smith, L. J., Evans, C. J., Lennon, D. J., & Bouret, J. C. 2003, ApJ, 588, 1039
Kahn, S. M., Leutenegger, M. A., Cottam, J., Rauw, G., Vreux, J.-M., den Boggende, A. J. F., Mewe, R., & Güdel, M. 2001, A&A, 365, L312
Kramer, R. H., Cohen, D. H., & Owocki, S. P. 2003, ApJ, 592, 532
Krolik, J. H., & Raymond, J. C. 1985, ApJ, 298, 660
Kurucz, R. L. 1979, ApJS, 40, 1
Lamers, H. J. G. L. M., & Leitherer, C. 1993, ApJ, 412, 771
Lanz, T., & Hubeny, I. 2003, ApJS, 146, 417
Lucy, L. B. 1982, ApJ, 255, 286
Lucy, L. B., & White, R. L. 1980, ApJ, 241, 300
Macfarlane, J. J., Waldron, W. L., Corcoran, M. F., Wolff, M. J., Wang, P., & Cassinelli, J. P. 1993, ApJ, 419, 813
MacGregor, K. B., & Cassinelli, J. P. 2003, ApJ, 586, 480
Martins, F., Schaerer, D., & Hillier, D. J. 2002, A&A, 382, 999
Massa, D., Fullerton, A. W., Sonneborn, G., & Hutchings, J. B. 2003, ApJ, 586, 996
Mewe, R., Raassen, A. J. J., Cassinelli, J. P., van der Hucht, K. A., Miller, N. A., & Güdel, M. 2003, A&A, 398, 203
Mewe, R., & Schrijver, J. 1975, Ap&SS, 38, 345
———. 1978a, A&A, 65, 99
———. 1978b, A&A, 65, 115
———. 1978c, A&AS, 33, 311
Miller, N. A., Cassinelli, J. P., Waldron, W. L., MacFarlane, J. J., & Cohen, D. H. 2002, ApJ, 577, 951
Mullan, D. J., & MacDonald, J. 2005, MNRAS, 356, 1139
Mullan, D. J., & Waldron, W. L. 2006, ApJ, 637, 506
Oskinova, L. M., Feldmeier, A., & Hamann, W.-R. 2004, A&A, 422, 675
———. 2006, MNRAS, in press (astro-ph/0603286)
Owocki, S. P., Castor, J. I., & Rybicki, G. B. 1988, ApJ, 335, 914
Owocki, S. P., & Cohen, D. H. 2001, ApJ, 559, 1108 (OC01)
———. 2006, ApJ, 648, 565
Porquet, D., Mewe, R., Dubau, J., Raassen, A. J. J., & Kaastra, J. S. 2001, A&A, 376, 1113
Pradhan, A. K. 1982, ApJ, 263, 477
Pradhan, A. K., & Shull, J. M. 1981, ApJ, 249, 821
Prinja, R. K., Barlow, M. J., & Howarth, I. D. 1990, ApJ, 361, 607
Puls, J., Markova, N., Scuderi, S., Stanghellini, C., Taranova, O. G., Burnley, A. W., & Howarth, I. D. 2006, A&A, 454, 625
Raassen, A. J. J., Cassinelli, J. P., Miller, N. A., Mewe, R., & Tepedelenlioğlu, E. 2005, A&A, 437, 599
Runacres, M. C., & Owocki, S. P. 2002, A&A, 381, 1015
Schulz, N. S., Canizares, C. R., Huenemoerder, D., & Lee, J. C. 2000, ApJ, 545, L135
Schulz, N. S., Canizares, C. R., Huenemoerder, D., & Tibbets, K. 2003, ApJ, 595, 365
Seward, F. D., Forman, W. R., Giacconi, R., Griffiths, R. E., Harnden, F. R., Jones, C., & Pye, J. P. 1979, ApJ, 234, L55
Waldron, W. L., & Cassinelli, J. P. 2001, ApJ, 548, L45 (WC01)
Waldron, W. L., Cassinelli, J. P., Miller, N. A., MacFarlane, J. J., & Reiter, J. C. 2004, ApJ, 616, 542
Young, P. R., Del Zanna, G., Landi, E., Dere, K. P., Mason, H. E., & Landini, M. 2003, ApJS, 144, 135